

Numerical simulation of rock dynamic fracturing and failure including microscale material randomness

Abedi, R., Omidi, O. and Clarke, P.L.

Department of Mechanical, Aerospace & Biomedical Engineering, The University of Tennessee Space Institute, TN, USA

Enayatpour, S.

Center for Petroleum and Geosystems Engineering, The University of Texas at Austin, TX, USA

Copyright 2016 ARMA, American Rock Mechanics Association

This paper was prepared for presentation at the 50th US Rock Mechanics/Geomechanics Symposium held in Houston, Texas, USA, 26-29 June 2016. This paper was selected for presentation at the symposium by an ARMA Technical Program Committee based on a technical and critical review of the paper by a minimum of two technical reviewers. The material, as presented, does not necessarily reflect any position of ARMA, its officers, or members. Electronic reproduction, distribution, or storage of any part of this paper for commercial purposes without the written consent of ARMA is prohibited. Permission to reproduce in print is restricted to an abstract of not more than 200 words; illustrations may not be copied. The abstract must contain conspicuous acknowledgement of where and by whom the paper was presented.

ABSTRACT: Realistic fracture simulations in rock as a heterogeneous brittle material with significant inherent randomness, requires the use of models that incorporate its inhomogeneities and statistical variability. Dynamic crack growth in rocks is generally associated with complex features such as crack path oscillations, microcracking and crack branching. We employ two approaches to address rock inhomogeneities for dynamic fracture simulations. First we model fractures explicitly with random size, location and orientation as natural pre-existing crack-like defects. Second, we use a probabilistic nucleation technique based on the Weibull model to implicitly incorporate creation of new cracks during the analysis. Both approaches can be used for the simulation of rocks for which the natural fractures are oriented in a specific angle, as in sedimentary rocks. We use the Spacetime Discontinuous Galerkin (SDG) method to efficiently and accurately capture complex fracture patterns observed in dynamic rock fracture. Specifically we employ a novel crack path tracking method, offered by the SDG method's powerful adaptive operations, to accurately model crack path oscillations, microcracking, and crack bifurcation. Our approach is applicable to rock fracture as well as problems where an induced major crack propagates and intersects natural fractures. Incorporation of macro-micro crack interactions can provide a more accurate estimation in hydrocarbon recovery in tight formations.

Acknowledgments: The authors gratefully acknowledge partial support for this work via the U.S. National Science Foundation (NSF), CMMI - Mechanics of Materials and Structures (MoMS) program grant number 1538332.

1 INTRODUCTION

Rocks are heterogeneous at different scales. At small grain scale, they are characterized by the presence of microcracks and granular microstructures. In fact, rocks contain a large number of randomly oriented zones of potential failure in the form of grain boundaries. At large mass scale, they are described by the presence of different rock types, faults and weak features such as fracture networks. These inhomogeneities affect the continuum level mechanical characteristics of rocks such as strength, toughness, and elasticity properties. However, mechanical properties of a solid can also be estimated by simulating its microstructure while it is loaded. In this context, failure in rock can be considered as the consequence of tensile and shear micro-fractures which progress within the microstructure and finally result in macro-fractures known as a failure state.

In many applications it is important to consider the natural discontinuities of rocks at different observation scales. Microcracks and pores in micro-scale or pre-existing fracture networks and faults in macroscale influence the formation of new discontinuities by joining and interacting with them. Rock blasting and hydraulic fracturing in

tight formations are two examples in which the goal of induced dynamic loadings is to increase the discontinuities. This issue needs to be properly addressed in computational simulations. The consequences of rock blasting which includes fracturing of the rock and fragment size distributions should be well estimated in design process. In hydraulic fracturing, an induced major crack propagates and intersects natural fractures which in turn are hydraulically loaded and extended to intersect other fissures and finally results in a new complicated fracture network. Incorporation of macro-micro crack interactions can highly improve computational estimations for the problems dealing with fracture in rocks. For example, models that do not include the interactions of main hydraulically loaded and propagated cracks with natural fissures often underestimate the hydrocarbon recovery from a tight reservoir. In contrast to these problems at which the aim of numerical evaluation is to maximize the fractures and cracks in rock, there are some events aiming to limit the formation of new fractures and prevent rock failure. Natural slopes, dams and underground openings are among the examples in which the existing natural fractures should be included in the simulations for their stability assessments.

Material heterogeneities and discontinuities can be ei-

ther *explicitly* or *implicitly* incorporated in a material model or computational approach for rock fracturing studies. In *explicit* approaches defects, microcracks, and other inhomogeneities are directly incorporated in the modeling. Lattice models provide a natural framework to explicitly model material inhomogeneities. Therein a lattice of elements as a network of particles are connected with springs [1] and heterogeneity is included through changing size and strength of lattice particles [2]. In the context of *Finite Element Methods* (FEMs), microcracks and other defects can be explicitly embedded in the discrete model implying that a considerably fine mesh is required to ensure that the existing microcrack density can be precisely represented.

In addition to FEMs that model the material as a continuum media, some other numerical methods such as *Discrete Element Method* (DEM) and *peridynamics* methods model the media as a collection of interacting particles. The material heterogeneities can be *explicitly* modeled by assigning different interaction properties, such as bond stiffness between the particles. There have also been several attempts to combine different computational approaches to maximize their flexibility in modeling complex rock media. For example, [3] proposed a combined finite-discrete element method (FDEM). In FDEM [4, 5], cracks are represented by discrete elements while the intact parts of the model are characterized by finite elements. This approach, however requires a contact algorithm to prevent overlapping of the bodies at any time [4].

While explicit approaches can provide an accurate representation of material heterogeneities, their application is often limited to small space and time scales due to need to directly resolve material microstructures. *Implicit* approaches, on the other hand incorporate the collective effect of microstructure into phenomenological models or continuum constitutive relations. For example, the probabilistic Weibull model [6, 7] provides a good representation of the size effect, *i.e.*, the decrease of failure strength as a specimen size increases, in brittle materials. Material microstructure can also be used to calibrate continuum fracture models such as the damage models in [8–11]. Homogenization approaches, on the other hand, derive macroscopic effective constitutive parameters by solving the underlying problem in a *Volume Element* (VE). If the VE is large enough to effectively homogenize material properties (if the material is macroscopically homogeneous), it is called a *Representative Volume Element* (RVE) which also is referred to as *Representative Elementary Volume* (REV) in rock mechanics. In contrast, *Stochastic Volume Elements* (SVEs), such as those in [12], are by design formulated for smaller VE sizes to preserve material heterogeneities and statistical variability. The random fields that can be realized from SVEs can be very effective and efficient for fracture analysis of brittle and quasi brittle materials since they maintain the microstructure variability, but average it to a larger and more manageable length scale.

Dynamic fracture of brittle and quasi-brittle materials such as rocks poses additional modeling and computational challenges. Dynamic fracture patterns are often more complicated; as a crack accelerates it starts to oscillate, em-

anate microcracks or interact with them, and eventually bifurcate to two or more macrocracks. The heavy interaction of the advancing macrocracks with in-situ microcracks, though increases levels of crack path oscillation and microcracking, makes their dynamic fracture more sensitive to microscale randomness. In addition, the increased number of moving crack tips and their shrinking fracture process zones, due to dynamic effects, poses serious challenges in their computational modeling.

In situ and dynamically propagating cracks can either be explicitly included in a fracture simulation or their collective effect being represented by a continuum model, such as a bulk damage model. With the former approach, in FEMs crack paths are either restricted between element boundaries or as in eXtended FEMs (XFEMs) [13–16] and generalized FEMs (GFEMs) [17, 18] being modeled by local element enrichment functions. Restricting crack paths to element boundaries can result in unreliable crack patterns and crack speeds when a fixed mesh is used. Although the XFEMs and GFEMs alleviate these problems, their formulation require enrichment functions that resemble analytical crack related fields within the elements. Any geometric or material complexities can make their derivation challenging. For example, due to the simplicity of LEFM theory, the majority of these methods represent crack tip fields using LEFM theory. Also, crack branching, intersection, and microcracking inside an element are examples of geometric complexities that require derivation of specific enrichment functions.

In this paper, we take two approaches to model material heterogeneities. In the explicit approach, we simulate a rock domain by directly incorporating in-situ mesoscale fractures in the computational domain. In the implicit method, a probabilistic nucleation model based on the Weibull model is proposed. The details of our fracture models are presented in §3. We use an *h*-adaptive *Space-time Discontinuous Galerkin* (SDG) finite element for elastodynamic simulation of rocks. Specifically, we employ the SDG method’s powerful spacetime adaptive operations to directly *track* complicated crack propagation paths in dynamic rock fracture. This provides an alternative approach to the powerful XFEM and GFEM methods in modeling complex rock fracture patterns. A short overview of the method is provided in §2. Finally, in §4 we qualitatively study the behavior of the explicit and implicit approaches and investigate the effect of certain aspects of rock microstructure on fracture patterns. An example will be the influence of angular bias of in-situ cracks, due to the bedding planes of sedimentary rocks or fracture response.

2 SPACETIME DISCONTINUOUS GALERKIN METHOD

This section briefly highlights the main features of the adaptive *Space-time Discontinuous Galerkin* (SDG) method along with adaptive operations that enable accurate simulation of rock fracture problems in §4.

2.1 Asynchronous and local spacetime solution scheme

Being a *Discontinuous Galerkin* (DG) finite element method, the SDG method employs element basis functions that are fully discontinuous across element boundaries. In addition, instead of employing a time marching scheme to advance the solution in time, we directly discretize the spacetime using unstructured grids that satisfy a special causality constraint as discussed below. Using discontinuous basis functions and direct discretization of spacetime with such special unstructured grids results in several unique properties when solving hyperbolic partial differential equations. Some of these features are the ability to achieve arbitrary high temporal orders of accuracy per element, a local and asynchronous solution scheme that lends itself to adaptive and parallel simulations, and excellent performance in resolving shocks and high gradient features in wave propagation problems. All these properties are highly important for the fracture problems considered herein.

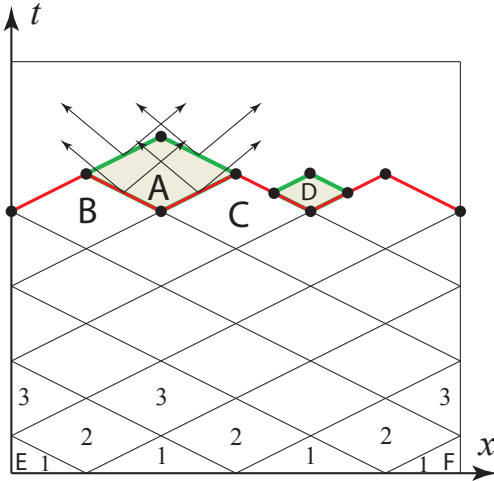


Figure 1: SDG Solution scheme on causal spacetime mesh in $1d \times \text{time}$. Reproduced from [19]

This SDG solver works with unstructured *causal* spacetime meshes shown in fig. 1 as a simple $1d \times \text{time}$ causal mesh. The inclined arrows indicate the characteristic directions where it is assumed the maximum wave speed is equal for the left- and right-moving waves. We impose a causality constraint on all facets moving in the spacetime mesh enabling a local solution scheme. The asymmetric causality dependency generates a partial element ordering by which the global solution can be computed locally, one element at a time. For example, the solution of element A depends only on the solution of earlier elements B and C because the inflow facets shown in red are shallower than the maximum wave speed. The solutions of B and C, however, do not depend on A. The level-1 elements depend only on initial conditions and boundary conditions for the elements E and F. The level-1 element solutions can be computed locally and in parallel. Thus, causal SDG meshes enable asynchronous, element-by-element solutions with linear complexity.

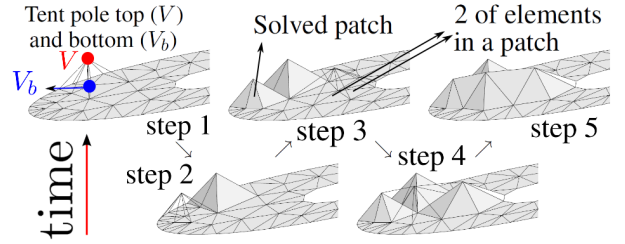


Figure 2: Patch-by-patch local solution process in $2d \times \text{time}$. Reproduced from [20]

In practice, we replace the individual elements with small clusters of simplex elements called *patches*, where only the exterior patch facets need to be causal; see fig. 2 for clusters of tetrahedral elements in $2d \times \text{time}$. The advancing-front meshing/solution procedure referred to by the *Tent Pitcher* algorithm [20] generates a sequence of causal spacetime patches, and we solve each one as soon as it is generated. Using this procedure, in each step the *Tent Pitcher* algorithm advances in time a vertex in the *front mesh* to define a local front update; This time advancing of a vertex, which is also called “tent-pitching” can be seen by erecting a tent-pole from the old front vertex V_b to the new front vertex V in fig. 2. The causality constraint limits the maximum time increment, *e.g.*, the temporal distance between V_b and V . A small group of spacetime simplices covers the region between the old and new fronts to form a new patch. We solve new patches as local problems and update the current front, until the entire spacetime analysis domain is solved. We observe the sequence of erecting and solving five small patches of elements in the figure. Please refer to [21] for more information about the SDG method.

2.2 Adaptive schemes for tracking cracks

We employ a highly efficient and flexible *h*-adaptive SDG method to accurately model complex fracture patterns in rocks. We use adaptive operations such as edge bisection, vertex deletion, and spacetime edge flip operation [20] for an *h*-adaptive formulation of elastodynamic problem [22]. In addition to the bulk energy dissipation error indicator in [22], we employ a secondary error indicator that specifically controls the energy error in rendering any interfacial fracture law [23]. Finally, by augmenting the spacetime adaptive operations, *e.g.*, smoothing and tilted tent poles, we have formulated an *adaptive crack tracking* approach that can align element boundaries with any given crack direction; *cf.* §3.3. The use of the dual error indicators, the SDG’s local and asynchronous solution scheme, and the crack tracking approach, result in highly accurate and efficient simulation of dynamic fracture problems for quasi-brittle materials and exact rendition of their complex fracture patterns. We note that while this *crack tracking* approach provides the same flexibility of XFEMs and GFEMs, it does not require the formulation of any enrichment functions. However, we believe that the full extension of this approach to 3D problems would be more challenging than that of XFEMs and GFEMs.

3 RANDOM FRACTURES AND ANGULAR BIAS

Two major strategies are employed herein to incorporate heterogeneity in rock fracturing. In the first approach, microcracks are explicitly embedded in the simulation. In the second technique, the influence of microcracks and existing natural fractures on the mechanical behavior of the rock is implicitly incorporated by employing a probabilistic nucleation model.

Our fracture algorithm has three parts: 1) Formation of *Active Crack Tips* (ACTs); 2) Crack propagation criterion for the ACTs; 3) Adapting the mesh to accommodate the crack growth directions. These features are addressed in the following subsections. Afterwards in §3.4, we briefly discuss how bedding planes can be incorporated in the simulations via enforcing a specific biased angle for the crack growth direction in implicitly embedded approach while in explicitly represented approach, the physical natural fractures can be simply distributed in a specific biased angle.

3.1 Active crack tip (ACT) formation

Depending on the material model pre-existing fractures, such as grain boundaries, and material interfaces, an in-situ microcrack can be explicitly incorporated in the physical model and simulation of the required information of size, orientation and location of all fracture are known a priori. Alternatively, the effects of defects and cracks can be homogenized to obtain effective elasticity or fracture properties. These properties are defined at the macroscopic continuum level and implicitly incorporate the effect of microscale defects. This study aims to simulate rock fracturing in both scenarios. In either case, the subsequent cracks in the domain can only propagate from *Active Crack Tips* (ACTs) whose formation depending on the employed approach is described below.

3.1.1 Explicitly Represented Approach (ERA)

In this method, the cracks are already included in the initial discretization. The tips of these cracks will become ACTs. Once the simulation starts, these crack tips will constantly be checked against the crack propagation criterion in §3.2 for potential crack propagation. To generate the initial cracks certain statistical properties of cracks must be specified. Crack length, denoted as l , follows a certain probability distribution such as the log normal or Weibull model. The density of initial cracks is defined by the crack density ratio,

$$\alpha = \frac{\sum_{i=1}^{nc} l_i^2}{A_c} \quad (1)$$

where A_c is the reference spatial area, nc is the number of cracks in A_c , and l_i are the crack lengths. We assume that the spatial position of cracks follows a uniform position. For the angular distribution of cracks we either assume

they are uniformly oriented or have certain preferred angles based on existing bedding planes. We use a “take and place” approach for forming the initial crack network. Each time, a crack from the given distribution is sampled and placed in the domain. If the crack intersects existing cracks, it is discarded. This process is continued until we reach the target crack density.

3.1.2 Implicitly Embedded Approach (IEA)

Fracture simulation of a domain with all of its micro and mesoscale defects can become too expensive. Alternatively, we can average or homogenize the effect of existing defects and microstructure as long as their sizes are small enough relative to a chosen *Volume Element* (VE) size so that homogenization techniques can be applied. Recent studies show that when material undergoes unstable stress-strain unloading and experiences fracture, instead of classical homogenization of bulk properties, the material response should be homogenized to an interfacial fracture model [24]. In addition, homogenization schemes that employ *Representative Volume Elements* (RVEs), rather than smaller volume elements known as *Stochastic Volume Elements* (SVEs), mask all material inhomogeneities which is not ideal for fracture simulations. Herein, instead of obtaining spatially inhomogeneous and statistically variable representation of material properties based on rigorous homogenization of microstructures by using SVEs we employ a phenomenological model to express fracture strength as a spatially uncorrelated random field. Transitioning to a sharp fracture model upon unstable strain-stress unloading, rather than using bulk homogenized values, is in accord with the approach proposed in [24]. In addition, using a probabilistic model ensures that we maintain material inhomogeneity and statistical variability as for example opposed to RVE-based homogenization schemes.

Our probabilistic crack nucleation model is based on the Weibull model [6, 7] which is very appropriate to express the probability of failure of brittle and to some extent quasi-brittle materials. The cumulative distribution function (CDF), *i.e.*, probability of failure, of a domain of size A and undergoing an effective stress s is given by,

$$P(s) = 1 - e^{-\frac{A}{A_0} \left(\frac{s - s_{\min}}{s_0} \right)^m} \quad (2)$$

where A_0 is a reference area, such as an experimental specimen size, for which the Weibull model is calibrated, s_0 is a strength scale, m is Weibull modulus (or shape parameter), and s_{\min} is the minimum fracture strength.

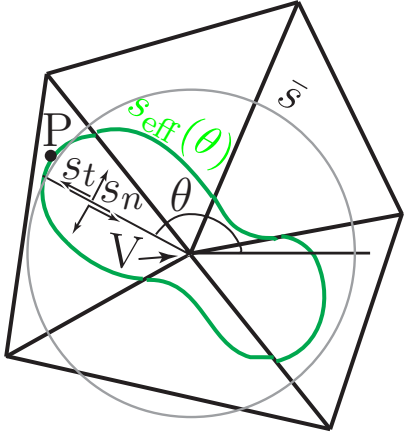


Figure 3: The angular distribution of effective stress s_{eff} and fracture strength \bar{s} around a patch tent pole top vertex V . The magnitude of these parameters for a given angle θ is mapped to a radial distance to V .

We use (2) to check the vertices of the discrete SDG mesh for crack nucleation. Figure 3 shows the spatial view of the top facets of a patch of elements that are solved locally in the SDG method. The vertex V corresponds to the tent pole ($V_b - V$) top of a sample patch shown in fig. 2. To investigate the probability of failure of the patch, we use its area A in (2) to fully characterized the CDF of fracture strength. Then, we sample a strength value \bar{s} from this calibrated distribution. This angular independent strength \bar{s} around the vertex V is shown in green in fig. 3. Next, we evaluate angular-dependent effect stress s_{eff} (discussed in §3.2) from individual finite elements in the patch. If s_{eff} for any direction such as that corresponding to P is larger than \bar{s} the vertex V is marked as an ACT and will be checked for potential crack extension the next times a patch is erected on the vertex V .

3.2 Crack growth criterion

To investigate whether a vertex on the active front becomes an ACT or an ACT will have a target propagation direction, we need to compute an effective stress around the vertex. We use the following definition of effective stress,

$$s_{\text{eff}}(\theta) = \sqrt{\langle s_n(\theta) \rangle_+^2 + \beta^2 s_t^2(\theta)} \quad (3)$$

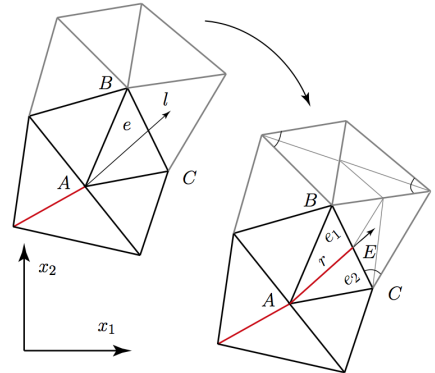
where β is the shear stress factor controlling mode mixity, and $s_n(\theta)$ and $s_t(\theta)$ are normal and shear components of traction on a potential crack extension angle θ as shown in fig. 3. The Macaulay positive part operator $\langle \cdot \rangle_+$ ensures that cracks do not propagate due to high compressive stresses and only the tensile part of s_n is incorporated in s_{eff} . We emphasize that if $|s_t| > \bar{s}/\beta$ crack nucleation / propagation criterion can still be satisfied under compressive stress states.

There are few aspects to discuss about assigning crack propagation directions. First, in ERA \bar{s} is a deterministic value for all vertices as material randomness is already modeled by the initial distribution of cracks. In IEA the randomly sampled \bar{s} for a nucleated ACT is used for its

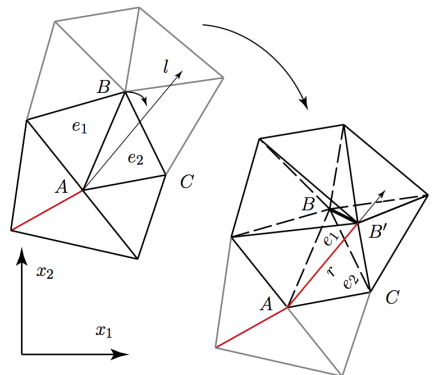
subsequent crack propagation checks. Second, we choose directions for crack propagation for which the effective stress is a local maximum and the value is larger than \bar{s} . For example, for the stress state shown in fig. 3 the crack propagates along VP direction.

3.3 Adaptive crack face alignment

When the crack propagation criterion from §3.2 is satisfied, the assigned crack direction(s) will be accommodated by the SDG's powerful adaptive operations in spacetime. Figure 4 illustrates a patch, where the vertex A as an ACT is assigned a crack propagation direction along the line l . Typically, l is not aligned with any of the element boundaries. There are two approaches to introduce an element boundary along the crack direction. In Figure 4(a), the vertex E is inserted on the edge BC such that AE is aligned with the crack direction. Subsequently, the space element e is subdivided to elements e_1 and e_2 . This operation is similar to the edge bisection procedure employed to refine the element e . In another situation where the direction of the element boundary AB is close to l , we align the edge AB with the crack direction by moving the vertex B to a point on line l . This can be achieved by erecting a tilted tent pole on vertex B such that the top vertex B' lies on line l as illustrated in Figure 4(b). More details about these two strategies can be found in [25].



(a) CST insertion on the opposite edge of the CST by a refinement operation.



(b) The spatial transition of a vertex by a tent pitching operation.

Figure 4: Extension of a crack in the space mesh through refinement and tent pitching operations

3.4 Angular bias due to bedding planes

To simulate domains containing bedding planes such as those in sedimentary rocks, we introduce angular bias in the initial crack formation or fracture strength. In ERA a nonuniform distribution of initial crack angles is assumed, *e.g.*, by having the highest probability densities along the bedding planes. In IEA, an angular profile for \bar{s} is chosen. The maximum strength about a vertex V is obtained from the Weibull probabilistic failure model in §3.1.2. Thus by having the profile of \bar{s} versus angle θ and its maximum value we fully characterize $\bar{s}(\theta)$ for a given vertex V . We note that the angular profile of \bar{s} can be spatially inhomogeneous and statistically random by using random variables to characterize for example the angle and value of minimum strength. One example of such model is presented in §4. The crack propagation direction from §3.2 is modified as now, both fracture strength $\bar{s}(\theta)$ and effective stress $s_{\text{eff}}(\theta)$ are angle dependent.

4 NUMERICAL RESULTS

In this section, we examine the influence of input material parameters on fracture patterns in rocks for both *Explicitly Represented Approach* (ERA) and *Implicitly Embedded Approach* (IEA). Figure 5 shows the geometry and loading of the problem considered. The rock sample is under in-situ hydraulic compressive stress $\sigma_H = 4.85$ MPa. All four sides of the computational domain are truncated with transmitting boundaries which are consistent with the ambient stress field σ_H . The domain dimensions are $L_x = 5\text{m}$, $L_y = 3\text{m}$, and the length of an initial crack length to the crack tip V is $L_c = 2\text{m}$. The material properties are: Young’s modulus $E = 20$ GPa and Poisson’s ratio $\nu = 0.2$. The faces of the initial crack are hydraulically loaded with a stress field that in one second is ramped from the ambient pressure to the sustained value of 19.4 MPa. All numerical results below are presented for a time slightly after the sustained loading value is reached. For all the simulations fracture along crack surfaces is modeled by an interfacial damage model from [26] with a characteristic fracture strength $\tilde{s} = 2$ MPa.

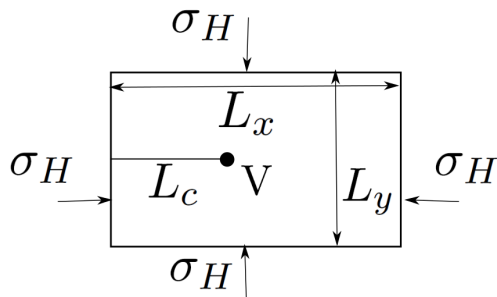
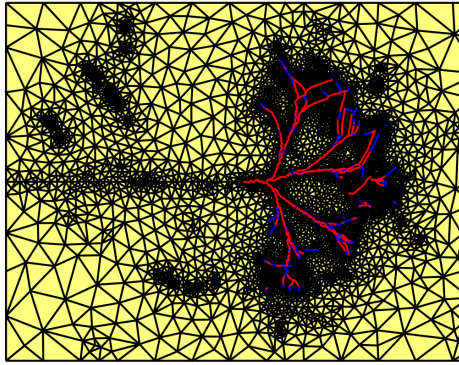


Figure 5: Schematic of the domain and loading condition for the numerical examples.

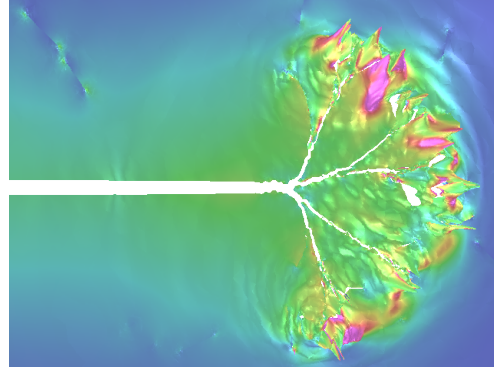
We first present the results from ERA where domains with different crack densities and angular distributions are subjected to the loading discussed above. In fig. 6, results

from domains with crack densities $\alpha = 0.1, 0.25$, and 0.50 are presented. Crack angles follow a uniform distribution. The *solution visualizations* on the right figs. 6(b,d,f) map stress and kinematic densities to color and height fields respectively. The *spatial visualizations* on the left figs. 6(a,c,e) show the spatial view of the SDG grids at a stage very close to the synchronized values used for solution visualizations. Since the front of elements in spacetime is not synchronized, the solution and spatial visualizations do not exactly match. The spatial mesh shows the crack pattern and the level of element refinement around the crack tips and crack paths. The newly generated cracks by crack propagation are shown in two colors. The red color denotes the complete failure of the crack surfaces while the blue color—which is mostly observed around the crack tips—corresponds to fracture process zones and other crack surfaces that have not experienced complete failure. The solutions for the lowest density $\alpha = 0.1$ are shown in figs. 6(a,b). The regions with high refinement ratios behind the fractured region in fig. 6(a) correspond to initially randomly generated cracks in the domain. The elastic waves emanated from the original crack tip at V and subsequently generated crack surfaces interacts with existing cracks. The interaction can induce small contact (stick and slip) and separation mode transitions on existing crack surfaces. We model these mode transitions with the models from [19]. We use very tight regularization values to ensure high accuracy of results, which explains high level of mesh refinement around existing cracks. The initial cracks that are in front of the hydraulically loaded propagating cracks from V , interact with the fracture pattern and start to propagate. Our analysis shows that they either start to propagate when a hydraulically loaded crack intersects them and transmits hydraulic load to their faces, or when the scattered waves from propagating cracks is large enough to initiate crack propagation from them. In either case, they eventually join the propagating cracks from V . As evident, the crack density is not high enough to greatly influence the propagating cracks. Figures 6(c,d) show the results for $\alpha = 0.1$. The fracture patterns do not change considerably compared to $\alpha = 0.1$, however more wave scattering off of microcracks behind the propagating cracks can be observed. Finally, the highest density results for $\alpha = 0.5$ are shown in 6(e,f). In this case we observe that existing cracks heavily interact with propagating cracks and change their path. Also, there is more wave scattering from the back side cracks. As for comparison, the space meshes corresponding to $\alpha = 0.1, 0.25, 0.50$ include 15697, 15838, and 23402 elements and 3270, 2417, and 2961 newly generated crack segments.

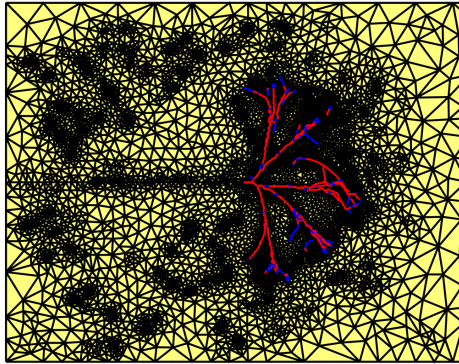
Figure 7 shows the results for ERA and same crack densities but when the initial cracks are oriented about 30 degree angle. The angular distribution of cracks follows a uniform distribution centered at 30 degrees with a span of 10 degrees. The purpose of this test to investigate how the angular bias of the initial fissures affect the macroscopic crack paths. Results for $\alpha = 0.1$ are shown in figs. 7(a,b). It appears that there are no major differences between this case and when the initial crack angles are uniformly distributed (unbiased orientation) from figs. 6(a,b). Same



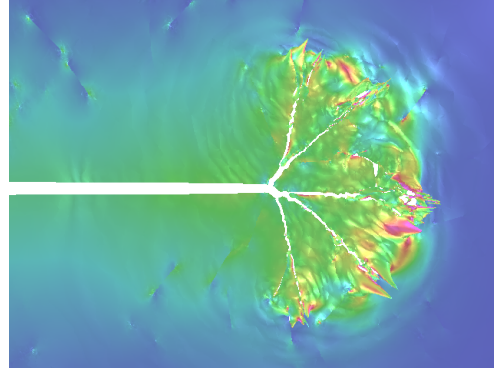
(a) Spatial mesh ($\alpha = 10$)



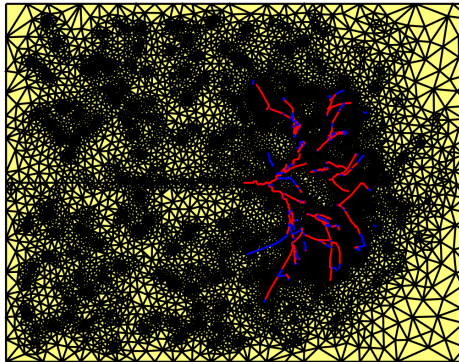
(b) Solution visualization ($\alpha = 10$)



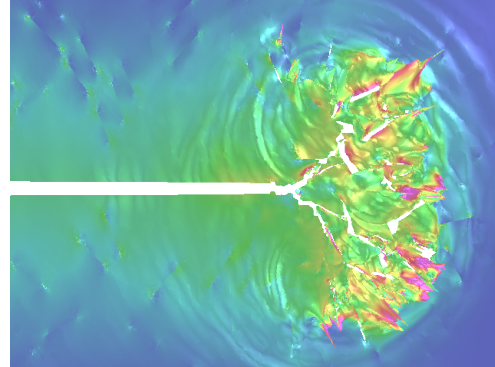
(c) Spatial mesh ($\alpha = 25$)



(d) Solution visualization ($\alpha = 25$)

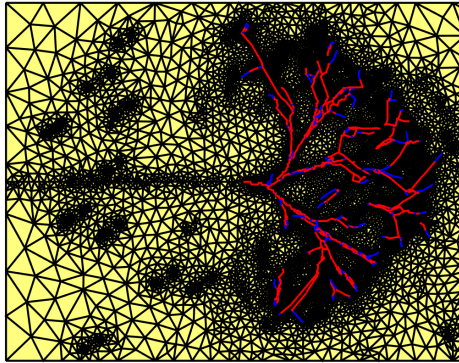


(e) Spatial mesh ($\alpha = 50$)

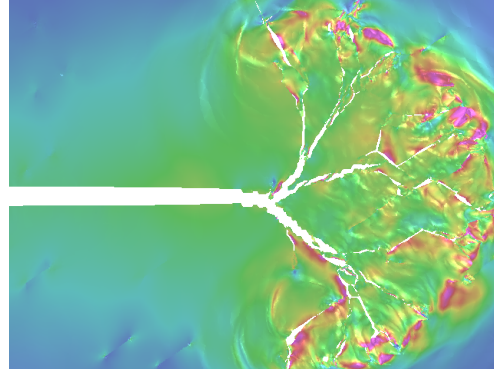


(f) Solution visualization ($\alpha = 50$)

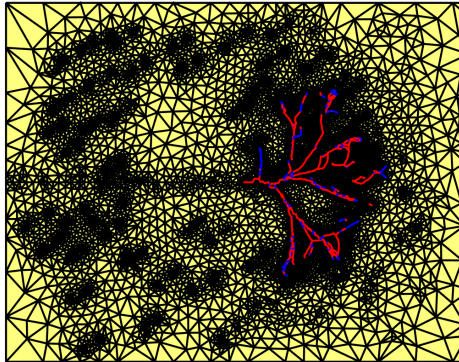
Figure 6: Solution of a hydraulically loaded crack interacting a randomly-distributed fracture network with different crack densities ($\alpha = 10, 25, 50$) in Explicitly Represented Approach



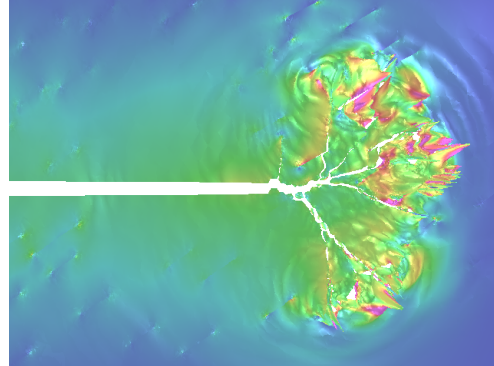
(a) Spatial mesh ($\alpha = 10$)



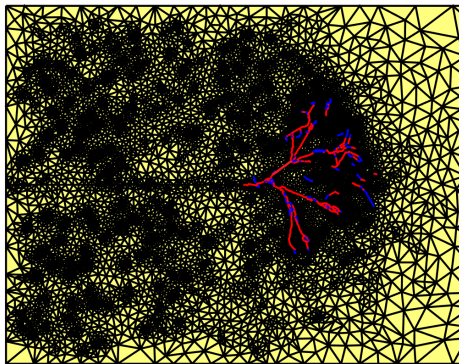
(b) Solution visualization ($\alpha = 10$)



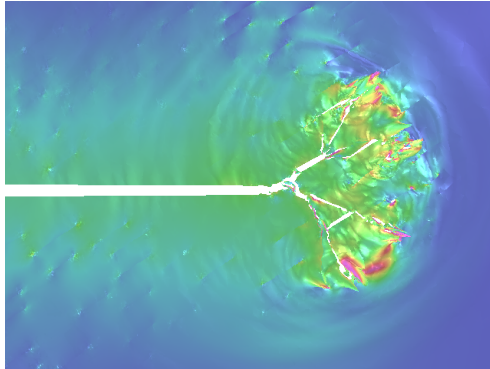
(c) Spatial mesh ($\alpha = 25$)



(d) Solution visualization ($\alpha = 25$)



(e) Spatial mesh ($\alpha = 50$)



(f) Solution visualization ($\alpha = 50$)

Figure 7: Solution of a hydraulically loaded crack interacting randomly-distributed fractures with with different crack densities ($\alpha = 10, 25, 50$) and biased angle of 30 in Explicitly Represented Approach

assertion can be made for higher crack density of $\alpha = 0.25$ in figs. 7(c,d). However, for the highest initial crack density $\alpha = 0.5$ in figs. 7(e,f) we observe that the macroscopic crack patterns is further influenced by initial crack orientations. For example, the upper major branch in figs. 7(e) has further advanced that the lower part and many crack angles in that segment are aligned close to 30 degrees. We anticipate that higher initial crack densities are required to heavily influence macroscopic crack patterns.

Next, we study the fracture patterns with IEA where the influence of initial defects and cracks in rock is modeled by the probabilistic nucleation approach from §3.1.2. The probabilistic crack nucleation approach based on the Weibull model from §3.1.2 has several parameters including the modulus m , strength scale s_0 , minimum strength s_{\min} , and reference area A_0 . We choose the following values for our simulations $m = 4$, $s_0 = 1.9$, $\tilde{s} = 3.8$ MPa and $s_{\min} = 0.25\tilde{s} = 0.5$ MPa. To change the likelihood of crack nucleation we vary the value of reference area A_0 to 1m^2 , 10m^2 , 100m^2 and 1000m^2 . While some of the values for A_0 can be unrealistic, our goal is to observe how such values may predict fracture patterns that are not expected in rocks. Other parameters such as m and s_0 will also be very influential as they alter the shape of the fracture strength probability distribution function and the scale of fracture, but we currently only investigate the influence of A_0 .

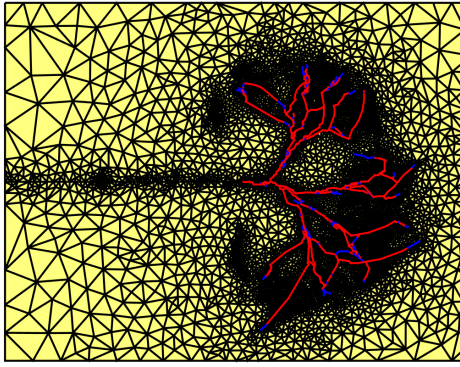
We first consider the case where the fracture strength \bar{s} , while being a random variable, is not a function of crack angle. That is, for a given position the fracture strength \bar{s} is the same for any potential crack propagation direction. As discussed in §3.1.2 the probability distribution of fracture strength \bar{s} for the tent pole top vertex V of a patch with area A is fully characterized by the Weibull model (2) from which a random strength for V is sampled. The results for varying levels of A_0 are shown in fig. 8. We observe that crack patterns for $A_0 = 1\text{m}^2$ from figs. 8(a,b) and $A_0 = 10\text{m}^2$ from figs. 8(c,d) show realistic fracture patterns for these dynamic fracture simulations. As expected, results from $A_0 = 1\text{m}^2$ have a more dense fracture pattern as smaller A_0 implies lower values for fracture strength from (2). However, as A_0 increases to 100m^2 in figs. 8(e,f) and 1000m^2 in figs. 8(g,h) it becomes extremely difficult to nucleate a crack and fracture patterns start to deviate from what is expected from quasi-brittle materials under dynamic loading. Specifically, for $A_0 = 1000\text{m}^2$ there is only one main crack that eventually bifurcates. The regions around the crack tips are under very high stress values but given the low probability of fracture, it is difficult to have any cracks to nucleate from these regions. As for comparison, the space meshes corresponding to $A_0 = 1\text{m}^2$, 10m^2 , 100m^2 , and 1000m^2 include 17872, 16358, 15582, and 7835 elements and 4339, 3278, 2220, and 634 newly generated crack segments.

Figure 9 shows the results with IEA but this time with angular dependent fracture strength $\bar{s}(\theta)$ where θ is the potential crack direction. It is assumed that $\bar{s}(\theta)$ has the lowest value of \bar{s}_{\min} at θ_{\min} and $\theta_{\min} + \pi$ and highest value \bar{s}_{\max} at $\theta_{\min} \pm \frac{\pi}{2}$. The value \bar{s}_{\max} is sampled similar to uniform angle values for \bar{s} in fig. 8. That is, it will be based

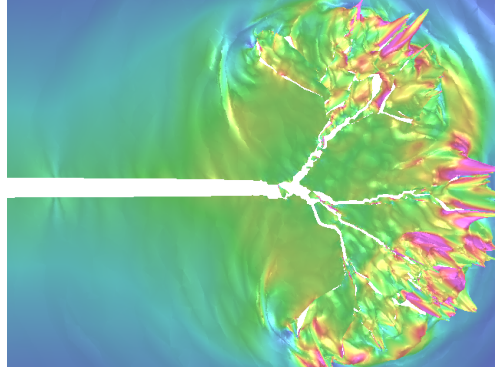
on the same Weibull parameters and local patch area A . However, the ratio $\frac{\bar{s}_{\min}}{\bar{s}_{\max}}$ is a random value with small variations around 0.1. The angle for minimum strength θ_{\min} is also a random value with the mean value of 30 degrees with ± 5 degrees variations. Similar to fig. 8, results are presented for $A_0 = 1\text{m}^2$, 10m^2 , 100m^2 , and 1000m^2 . We emphasize that all parameters are the same between angular uniform \bar{s} in fig. 8 and biased $\bar{s}(\theta)$ herein, for the same A_0 the results from $\bar{s}(\theta)$ represent a weaker rock due to having around 10% lower strength about 30 degrees.

Figures 9(a,b) show the results for $A_0 = 1\text{m}^2$. Such a low value for A_0 implies a very weak material as from (2) for a patch area $A \ll A_0$ the probability of failure, *i.e.*, crack nucleation, becomes very high for relatively small stress values. The applied hydraulic load on initial crack surfaces sends in compressive longitudinal stress waves to the top and bottom on the hydraulically loaded crack surface. This in turn breaks the hydraulic stress state in the rock and induces large enough shear stresses. Consequently effective stresses from (3) signal crack nucleation from the already low sampled fracture strengths. This results in widespread crack nucleation and propagation along the weakest direction, *i.e.*, about 30 degrees, on both sides of the main crack. Interestingly, the majority of these cracks undergo a small amount of failure, evident from the blue color of cracks in fig. 9(a). The reason is that there is not sufficient energy to bring all the fracture surfaces to full damage. As shown in fig. 9(b) only a small fraction of these cracks exhibit major separation or sliding. Another important aspect is the under-developed fracture network propagated in front of the main crack tip. Again there are many cracks but very small fraction of them exhibit major damage. The same behavior can be observed for $A_0 = 10\text{m}^2$ in 9(b) 9(c,d), although due to the overall higher sampled fracture strengths $\bar{s}(\theta)$ there are many more points which will not be nucleated. This makes the probabilistic aspect of the model more evident. This is opposed to $A_0 = 1\text{m}^2$ where regardless of the details for the probabilistic model almost all points get nucleated due to very low sampled $\bar{s}(\theta)$. Another interesting feature for $A_0 = 10\text{m}^2$ is the introduction of cracks with angles other than 30 degrees on the sides of the main crack; specifically, we observe some cracks along 150 degrees on the top side in fig. 9(c).

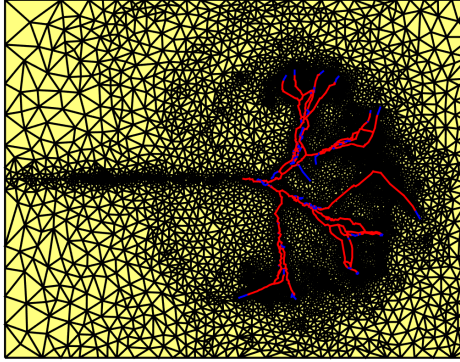
The results for $A_0 = 100\text{m}^2$ and $A_0 = 1000\text{m}^2$ are shown in fig. 9(e) to fig. 9(h). As expected due to the lower probability of crack nucleation from mesh grid vertices, we observe fewer cracks nucleated and propagated and that most of them experience full damage. We still observe few cracks propagated on the two sides of the main crack along about 30 degree angles. The random location of these cracks is a consequence of employing a probabilistic crack nucleation model. In comparison between uniform angular distribution of \bar{s} in fig. 8(e) to fig. 8(h) and the current results for angular dependent strength $\bar{s}(\theta)$ we observe much more fracture formation in the latter case for both $A_0 = 100\text{m}^2$ and 1000m^2 . We contribute this to having generally smaller fracture strengths, especially about tenfold smaller $\bar{s}(\theta)$ for $\theta \approx 30^\circ$. To quantify this, we observe that for $\bar{s}(\theta)$ the space meshes corresponding



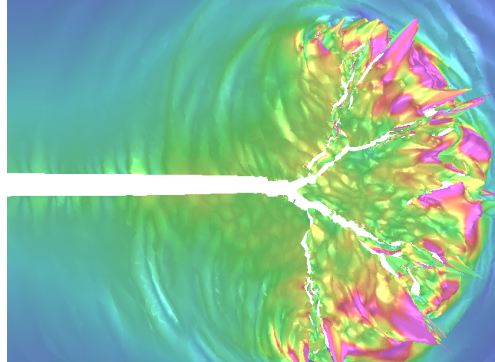
(a) Spatial mesh ($A_0 = 1$)



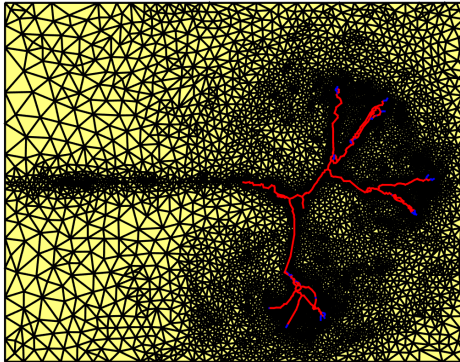
(b) Solution visualization ($A_0 = 1$)



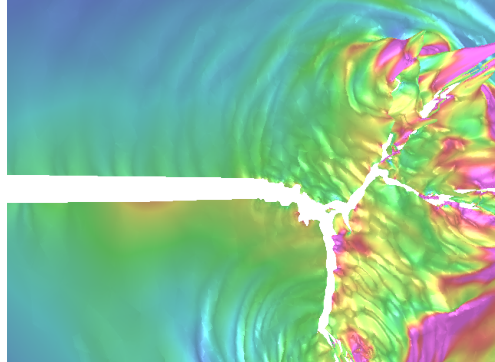
(c) Spatial mesh ($A_0 = 10$)



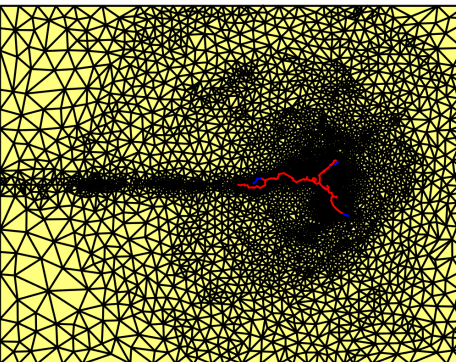
(d) Solution visualization ($A_0 = 10$)



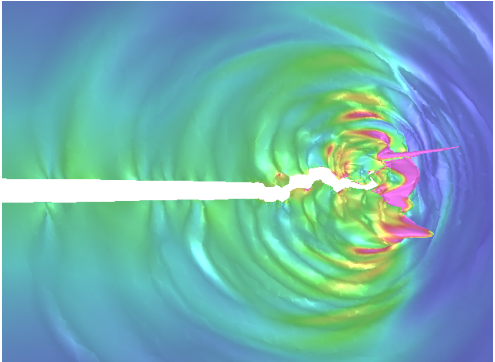
(e) Spatial mesh ($A_0 = 100$)



(f) Solution visualization ($A_0 = 100$)

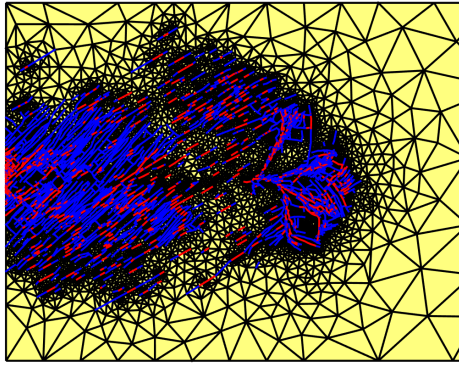


(g) Spatial mesh ($A_0 = 1000$)

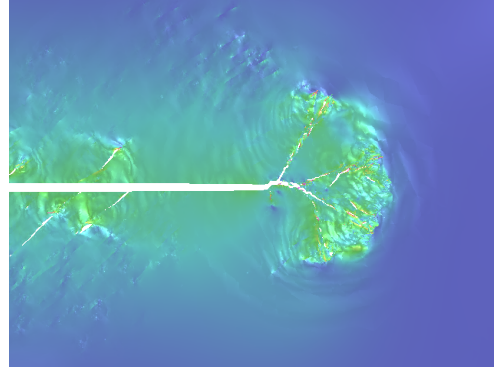


(h) Solution visualization ($A_0 = 1000$)

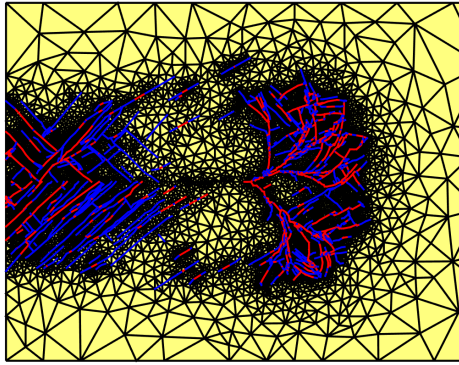
Figure 8: Solution of a hydraulically loaded crack interacting a randomly-distributed fracture network with different reference areas ($A_0 = 1, 10, 100, 1000$) in Implicitly Embedded Approach



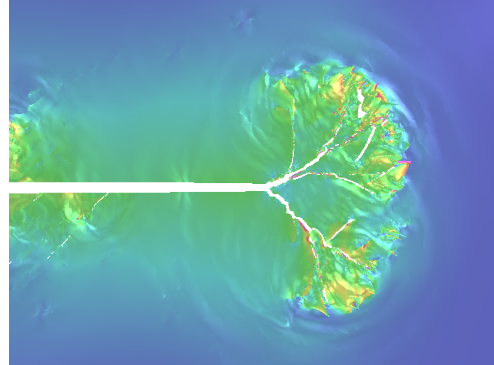
(a) Spatial mesh ($A_0 = 1$)



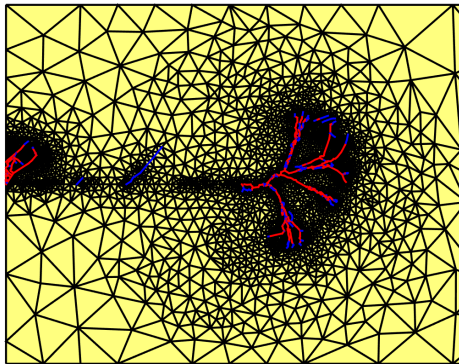
(b) Solution visualization ($A_0 = 1$)



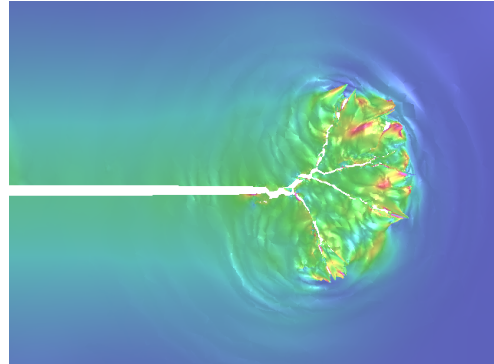
(c) Spatial mesh ($A_0 = 10$)



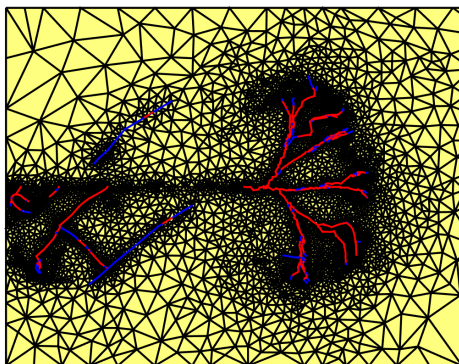
(d) Solution visualization ($A_0 = 10$)



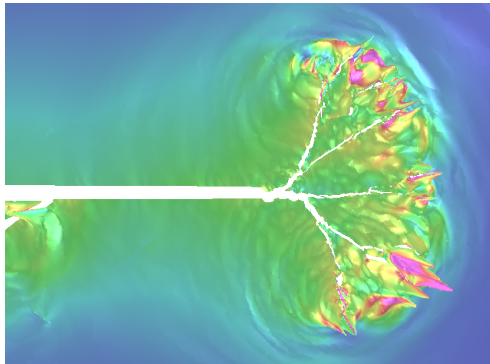
(e) Spatial mesh ($A_0 = 100$)



(f) Solution visualization ($A_0 = 100$)



(g) Spatial mesh ($A_0 = 1000$)



(h) Solution visualization ($A_0 = 1000$)

Figure 9: Solution of a hydraulically loaded crack interacting a randomly-distributed fracture network with different reference areas ($A_0 = 1, 10, 100, 1000$) and biased angle of 30 in Implicitly Embedded Approach

to $A_0 = 1\text{m}^2, 10\text{m}^2, 100\text{m}^2$, and 1000m^2 include 31717, 27453, 12608, and 14558 elements and 17137, 10530, 3839, and 3513 newly generated crack segments. That is, with angular dependent $\bar{s}(\theta)$ we observed from two to six times more crack segments compared to uniform strength for this particular study.

5 CONCLUSIONS

Fracture models that ignore material inhomogeneity or statistical variability can fail in capturing certain characteristic behaviors of quasi-brittle materials such as rocks. The use of homogeneous fracture and elastic properties fail to capture the correct fracture response when stress state is rather uniform, mainly due to the fact that all points experience almost the same stress state and would fail simultaneously. This continuum level shortcoming can manifest itself in predicting fracture formation between (or inside) all elements almost independently of the resolution of the spatial grid when the stress field is rather uniform.

We proposed two different approaches to take material inhomogeneity and statistical variability into account. In the *Explicitly Represented Approach* (ERA) we explicitly generate cracks in a computational domain based on a given statistical description of in-situ fissures. In *Implicitly Embedded Approach* (IEA) the influence of defect and microcrack distribution is implicitly incorporated in a phenomenological nucleation model. Some unique computational aspects of our approach are using powerful adaptive operations in spacetime to exactly accommodate any crack direction dictated by a fracture propagation criterion. The interaction of these cracks with pre-existing fissures can become quite complex as shown in figs. 6(e-f). The adaptive SDG finite element method is also very robust to solve highly dense fracture networks as in fig. 9(a). Moreover, we studied the influence of in-situ crack density by directly incorporating it with ERA and modifying the Weibull model parameters, specifically the reference area A_0 , with IEA. Finally, we observed different qualitative responses when rocks with preferred fracture planes were modeled. In the ERA the in-situ fractures did not heavily influenced macroscopic fracture patterns for crack densities α smaller than 0.5 while with IEA fracture network was heavily influenced by the weakest fracture planes, especially for the weakest $\bar{s}(\theta)$ corresponding to $A_0 = 1\text{m}^2$ and 10m^2 .

We emphasize that the statistical models used in the current study are not based on any actual representation of rock inhomogeneities. Natural extensions to this work include formulating the crack statistical distribution of in-situ fractures for ERA based on experimental observations. For IEA, we can homogenize the effect of microscopic defects and cracks into phenomenological elasticity and fracture parameters. A key step would be the use of *stochastic volume elements* (SVEs) rather than *representative volume elements* (RVEs) to maintain the rock's spatial inhomogeneities and statistical variability. Alternatively a variety of geostatistical models, see [27] for a review, can be very useful in populating a domain with in-situ fractures or for

formulating phenomenological models for the distribution of fracture strength and elastic properties.

REFERENCES

- [1] Schlangen, E. and E.J. Garboczi (1997) Fracture simulations of concrete using lattice models: Computational aspects. *Engineering Fracture Mechanics*, **57**, 319–332.
- [2] Li, H.L., Y.L. Bai, M.F. Xia, F.J. Ke, and X.C. Yin (2000) Damage localization as a possible precursor of earthquake rupture. *pure and applied geophysics*, **157**, 1929–1943.
- [3] Munjiza, A.A. (2004) *The Combined Finite-Discrete Element Method*. John Wiley & Sons.
- [4] Mahabadi, O. K., A. Lisjak, A. Munjiza, and G. Grasselli (2012) Y-geo: New combined finite-discrete element numerical code for geomechanical applications. *International Journal of Geomechanics*, **12**, 676–688.
- [5] Mahabadi, O.K., B.S.A. Tatone, and G. Grasselli (2014) Influence of microscale heterogeneity and microstructure on the tensile behavior of crystalline rocks. *Journal of Geophysical Research: Solid Earth*, **119**, 5324–5341.
- [6] Weibull, W. (1939) A statistical theory of the strength of materials. *R. Swed. Inst. Eng. Res.*, p. Res. 151.
- [7] Weibull, W. (1951) A statistical distribution function of wide applicability. *Journal of Applied Mechanics*, **18**, 293–297.
- [8] Taylor, Lee M., Er-Ping Chen, and Joel S. Kuszmaul (1986) Microcrack-induced damage accumulation in brittle rock under dynamic loading. *Computer Methods in Applied Mechanics and Engineering*, **55**, 301 – 320.
- [9] Homand-Etienne, F., D. Hoxha, and J.F. Shao (1998) A continuum damage constitutive law for brittle rocks. *Computers and Geotechnics*, **22**, 135–151.
- [10] Shao, J.F. and J.W. Rudnicki (2000) A microcrack-based continuous damage model for brittle geomaterials. *Mechanics of Materials*, **32**, 607 – 619.
- [11] Lu, Y.L., D. Elsworth, and L.G. Wang (2013) Microcrack-based coupled damage and flow modeling of fracturing evolution in permeable brittle rocks. *Computers and Geotechnics*, **49**, 226–44.
- [12] Koyama, Tomofumi and Lanru Jing (2007) Effects of model scale and particle size on micro-mechanical properties and failure processes of rocks—a particle mechanics approach. *Engineering Analysis with Boundary Elements*, **31**, 458 – 472, innovative Numerical Methods for Micro and Nano Mechanics and Structures - Part I Innovative Numerical Methods for Micro and Nano Mechanics and Structures - Part I.

- [13] Belytschko, T. and T. Black (1999) Elastic crack growth in finite elements with minimal remeshing. *International Journal for Numerical Methods in Engineering*, **45**, 601–620.
- [14] Moes, N., J. Dolbow, and T. Belytschko (1999) A finite element method for crack growth without remeshing. *International Journal for Numerical Methods in Engineering*, **46**, 131–150.
- [15] Dolbow, J., N. Moes, and T. Belytschko (2000) Discontinuous enrichment in finite elements with a partition of unity method. *International journal for numerical methods in engineering*, **36**, 235–260.
- [16] Remmers, J. J. C., Rene de Borst, and A. Needleman (2003) A cohesive segments method for the simulation of crack growth. *Computational Mechanics*, **31**, 69–77.
- [17] Strouboulis, T., I. Babuška, and K. Copps (2000) The design and analysis of the generalized finite element method. *Computer Methods in Applied Mechanics and Engineering*, **181**, 43–69.
- [18] Strouboulis, T., K. Copps, and I. Babuška (2001) The generalized finite element method. *Computer Methods in Applied Mechanics and Engineering*, **190**, 4081–4193.
- [19] Abedi, Reza and Robert B. Haber (2014) Riemann solutions and spacetime discontinuous Galerkin method for linear elastodynamic contact. *Computer Methods in Applied Mechanics and Engineering*, **270**, 150 – 177.
- [20] Abedi, Reza, Shuo-Heng Chung, Jeff Erickson, Yong Fan, Michael Garland, Damrong Guoy, Robert Haber, John M. Sullivan, Shripad Thite, and Yuan Zhou (2004) Spacetime meshing with adaptive refinement and coarsening. *Proceedings of the Twentieth Annual Symposium on Computational Geometry*, June 9-11, pp. 300–309, SCG '04, ACM.
- [21] Abedi, Reza, Robert B. Haber, and Boris Petracovici (2006) A spacetime discontinuous Galerkin method for elastodynamics with element-level balance of linear momentum. *Computer Methods in Applied Mechanics and Engineering*, **195**, 3247–3273.
- [22] Abedi, R., R. B. Haber, S. Thite, and J. Erickson (2006) An h -adaptive spacetime-discontinuous Galerkin method for linearized elastodynamics. *Revue Européenne de Mécanique Numérique (European Journal of Computational Mechanics)*, **15**, 619–642.
- [23] Abedi, Reza, Morgan A. Hawker, Robert B. Haber, and Karel Matouš (2009) An adaptive spacetime discontinuous Galerkin method for cohesive models of elastodynamic fracture. *International Journal for Numerical Methods in Engineering*, **1**, 1–42.
- [24] Nguyen, Vinh Phu, Oriol Lloberas-Valls, Martijn Stroeve, and Lambertus Johannes Sluys (2011) Homogenization-based multiscale crack modelling: From micro-diffusive damage to macro-cracks. *Computer Methods in Applied Mechanics and Engineering*, **200**, 1220–36.
- [25] Omid, O., R. Abedi, and S. Enayatpour (2015) An adaptive meshing approach to capture hydraulic fracturing. *In Proceedings of the 49th US Rock Mechanics/Geomechanics Symposium*, pp. ARMA 15–572.
- [26] Abedi, Reza (2010) *Spacetime damage-based cohesive model for elastodynamic fracture with dynamic contact*. Ph.D. thesis, Department of Theoretical and Applied Mechanics, University of Illinois at Urbana-Champaign.
- [27] Dowd, Peter A., Chaoshui Xu, Kanti V. Mardia, and Robert J. Fowell (2007) A comparison of methods for the stochastic simulation of rock fractures. *Mathematical Geology*, **39**, 697–714.